Mapping of Photon Distribution and Imaging of MR-Derived Anatomically Accurate Optical Models of the Female Breast

San-Lian S. Barbour, *Randall L. Barbour, Ping C. Koo,

*Harry L. Graber, and *Jenghwa Chang

Bioimaging Sciences Corporation, 64 Burnett Terrace, West Orange, NJ 07052

and

*Departments of Pathology and Biophysics,

SUNY Health Science Center at Brooklyn, Brooklyn, NY 11203

Abstract

We have computed optical images of the female breast based on analysis of tomographic data obtained from simulated time-independent optical measurements of anatomically accurate maps derived from segmented 3-D magnetic resonance (MR) images. Images were segmented according to the measured MR contrast levels for fat and parenchymal tissue from T1 weighted acquisitions. Computed images were obtained from analysis of solutions to the forward problem for breasts containing "added pathologies", representing tumors, to breasts lacking these inclusions. Both breast size and its optical properties have been examined over a range of values, including large and small breasts and optical scattering lengths smaller and larger than those expected in tissue. In each case, two small simulated tumors (approximately 0.1% of breast volume) were "added" to the background tissue. Values of absorption and scattering coefficients of the tumors have been examined that are both greater and less than the surrounding tissue.

Detector responses and the required imaging operators were computed by numerically solving the diffusion equation for inhomogeneous media. Detectors were distributed uniformly, in a circular fashion, around the breast in a plane positioned parallel and half-way between the chest wall and the nipple. A total of 20 sources were used, and for each 20 detectors. Reconstructed images were obtained by solving a linear perturbation equation derived from transport theory. Three algorithms were tested to solve the perturbation equation and include, the methods of Conjugate Gradient Decent (CGD), Projection onto Convex Sets (POCS), and Simultaneous Algebraic Reconstruction Technique (SART). Results obtained showed that in each case, high quality reconstructions were obtained. The computed images correctly resolved and identified the spatial position of the two tumors. Additional studies showed that computed images were stable to large systematic errors in the imaging operators and to added noise. Further, examination of the computed detector readings indicate that images of tissue up to approximately 10 cm in thickness should be possible.

The results reported are the first to demonstrate that high quality images of small added inclusions can be obtained from anatomically accurate models of thick tissues having arbitrary boundaries based on the analysis of diffusely scattered light.

1. Introduction

Recently, there has been a significant interest in the possibility of imaging the interior optical properties of thick tissues using NIR laser sources [1]. Light propagating through tissue is intensely scattered. For thick tissue structures, such as a breast, this causes the intensity of unscattered photons to become vanishingly small. As a result, image recovery efforts must consider evaluation of highly scattered photons.

The inverse scattering problem has long been recognized as being notoriously difficult. From electromagnetic theory we learn that solutions to this problem can, in principal, be obtained from formulations derived from Maxwell's equation. In practice, however, because of the intense scattering of optical photons in tissue, the computational complexity of these approaches quickly renders intractable any serious examination of optical data from tissue. An alternative formulation, also capable of accounting for the effects of scattering, is *transport theory*. This approach treats

0-8194-1736-X/95/$6.00

penetrating photons as particles. The principal advantage of this scheme is its ready ability to treat situations where scattering is the dominant mechanism affecting photon migration. The suitability of this formulation under these conditions, and its related approximation, the diffusion equation, are well known to many who study neutron transport, and has been successfully applied for many years to problems involving reactor shielding and weapons development.

Several years ago, Aronson and Barbour [2,3], described a 3-D image recovery scheme derived from transport theory that is suitable for examining the interior properties of opaque dense scattering media. The approach considers a tomographic type measurement scheme, similar to that commonly employed in other imaging modalities, and requires solution of a linear perturbation equation. The principal difference of this method compared to, for example, x-ray CT, is the use of imaging operators that explicitly take into account the effects of multiple scattering. The physical interpretation of these operators is that they represent the spatial probability distribution of photons launched from a source that enter a specified detector. Phenomenologically, a map of this distribution looks similar to a cloud. It has fuzzy boarders, with some regions more dense than others, usually in the vicinity of the source and detector. Use of these functions for imaging dense scattering media can be considered analogous as to how the straight line paths taken by x-rays are evaluated in CT imaging.

Independently, Singer *et al.* in 1990 [4] and Arridge *et al.* in 1991 [5] also reported formulations derived from transport theory. The approaches of Barbour *et al.* [6] and Arridge *et al.* [7] require the solution of linear perturbation equations that make use of specified reference states. The numerical methods used here are similar to approaches used in impedance tomography [8] and the travel–time seismography problem [9]. The principal difference relates to the interpretation of the imaging operator. An update of the imaging operator can be attempted, in which case the method can be described as nonlinear. The method of Singer *et al.* [4] does not rely on a reference medium, but instead attempts to directly recover the image by iteratively updating a propagation matrix based on an analytical approach. Since these early reports, the use of perturbation methods derived from transport theory has been adopted by several groups [1].

Recently, we have described an efficient and practical approach for optimizing data collection and analysis strategies for optical measurements involving *thick tissue structures* [10,11]. The basic approach considers the use of priors to derive anatomically accurate optical (AAO) models of tissues. This is accomplished by assignment of optical coefficients to tissue types identified from segmented, 3-D MRI images. We choose the MRI method because of the excellent contrast observed for soft tissues. By assigning previously reported values of optical coefficients to identified tissue types, estimates of the photon distributions in tissues having nonuniform composition and boundaries can be directly computed. Simulations of tomographic illumination schemes can readily be performed for native tissues and those containing "added pathologies", thereby permitting assessment of the suitability of various data collection and analysis schemes.

In this study we have extended preliminary reports [10,11] and consider optical models of the female breast that vary in volume and range of absorption and scattering coefficients for the background tissues and simulated tumors. In each case solutions to the forward problem were computed for simulated tomographic measurements using a time-independent source. Detector readings and imaging operators were obtained from solutions to the diffusion equation for inhomogeneous media. The quality of reconstructed images were examined as a function of the algorithm used and systematic errors in the imaging operators and added noise to the detector readings.

2. Methods

We have previously derived a linear perturbation model for imaging differences in the optical coefficients for an arbitrary medium [6]. Briefly, let the target medium be discretized into J voxels and $\Delta\mu_{aj}$ be the volume–averaged perturbation of , for example, the absorption cross section in voxel j. Let I be the total number of source–detector pairs and $\Delta\phi_i$ be the detector reading for the i^{th} source–detector pair; then Eq. (1) can be written as a system of linear equations:

$$\Delta\Phi = \mathbf{W}\Delta\mu_a, \tag{1}$$

where:

$$\Delta\Phi = \begin{bmatrix} \Delta\phi_1 \\ \Delta\phi_2 \\ \vdots \\ \Delta\phi_I \end{bmatrix}, \quad \mathbf{W} = \begin{bmatrix} w_{11} & w_{12} & \cdots & w_{1J} \\ w_{21} & w_{22} & \cdots & w_{2J} \\ \vdots & \vdots & \ddots & \vdots \\ w_{I1} & w_{I2} & \cdots & w_{IJ} \end{bmatrix}, \quad \Delta\mu_a = \begin{bmatrix} \Delta\mu_{a1} \\ \Delta\mu_{a2} \\ \vdots \\ \Delta\mu_{aJ} \end{bmatrix}.$$

The calculation of w_{ij} is performed by discretizing the continuous weight function in Eq. (1):

$$w_{ij} = \sum_{k=1}^{K} G^S_{ijk} G^D_{ijk} \tag{2}$$

where K is the total number of discretized directional components and:

$$G^S_{ijk} = \frac{1}{V_j} \int_{V_j} \int_{\Omega_k} \overline{G}(\mathbf{r}', \Omega'; \mathbf{r}_{Si}, \Omega_{Si}; 0)\, d\Omega'\, d^3r$$

$$G^D_{ijk} = \frac{1}{V_j} \int_{V_j} \int_{\Omega_k} \overline{G}(\mathbf{r}', \Omega'; \mathbf{r}_{Di}, \Omega_{Di}; 0)\, d\Omega'\, d^3r$$

are the averaged Green's function in voxel j and direction component k for the i^{th} source–detector pair. G^S_{ijk} and G^D_{ijk} are also called the normalized direct and adjoint intensities, respectively. K is taken to be 1 in this study, that is, the integrated intensity over 4π steradians in each voxel was used for weight function calculation.

The inverse problem can also be stated as follows: given a set of source–detector pairs, the perturbed detector readings $\Delta\Phi$, and the pre–calculated weight function $\mathbf{W}$, find the perturbation of the macroscopic absorption cross sections $\Delta\mu_a$ of the target medium.

3–D MR Breast Phantom

A series of 24 sagittal MR breast images were obtained using a GE Signa MR system. The fast spin echo (T_R = 4000 msec, T_E = 112 msec, 3 mm thickness) technique was used, with and without fat and water saturation. Surface coils were used, to obtain better uniformity of the field. Figure 1 shows a sagittal section through one such image. This series of sagittal sections was then used as the reference medium in image reconstructions. Prior to evaluating the MR data for computation of photon intensities, spatial averaging was performed to yield a 3-D image of dimension 49x35x24.

Each pixel in the digitized MR image had an assigned integer value in the range 1–256. The breast was segmented into two different tissue types – "fat" and "parenchyma." The segmentation was accomplished via a simple thresholding technique, in which all MR image pixels possessing image intensities ≤ 128 were assumed to be one tissue type and all those with image intensities > 128 were assumed to be the other type. Figure2 shows a sagittal section of a segmented image. Each tissue type was then assigned a set of optical properties – μ_a and μ_s', the absorption and reduced scattering cross-section, respectively. Two "pathologies" were introduced by assigning different μ_a and μ_s' values to selected voxels in two regions. A schematic of this is illustrated in Figure 3. The values listed in Table 1 identify the range of optical properties used. Although the scattering and absorption cross sections of the pathologies both were perturbed, images were reconstructed according to a model that assumes perturbations in only the absorption cross sections.

Solutions of the direct problem for 3–D MR breast data were computed using a relaxation code. Relaxation [12] is a numerical method commonly used to solve the diffusion equation, which is an approximation to the transport equation. The continuous diffusion equation with inhomogeneous diffusion constant $D(\mathbf{r})$ is:

$$\frac{1}{c_n}\frac{\partial}{\partial t}\Phi(\mathbf{r},t) - \nabla\cdot[D(\mathbf{r})\nabla\Phi(\mathbf{r},t)] + \mu_a(\mathbf{r})\Phi(\mathbf{r},t) = S(\mathbf{r},t), \tag{13}$$

Figure 1

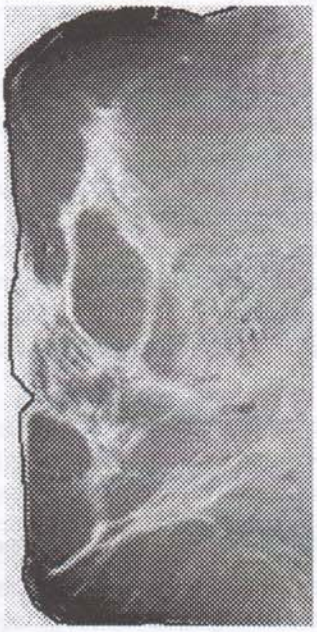

Sagittal Slice of Breast

Figure 1. Sagittal slice of female breast. Image shown is one of 24 slices obtained. All were used to compute solutions of the forward problem.

Figure 2

Segmented

Figure 2. Illustration of segmentation of one sagittal cut of MR breat images. The fat and parenchyma tissues were segmented using simple thresholding.

Figure 3

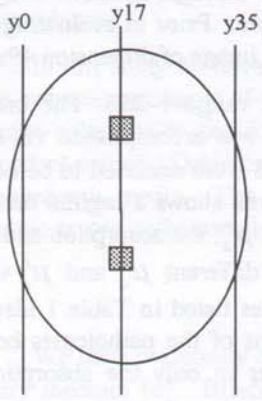

Figure 3. Illustration of position of "added pathologies". MR image of slice y17 is shown in Figure 1. See Table 1 for description of assigned optical properties used in these studies.

Figure 4

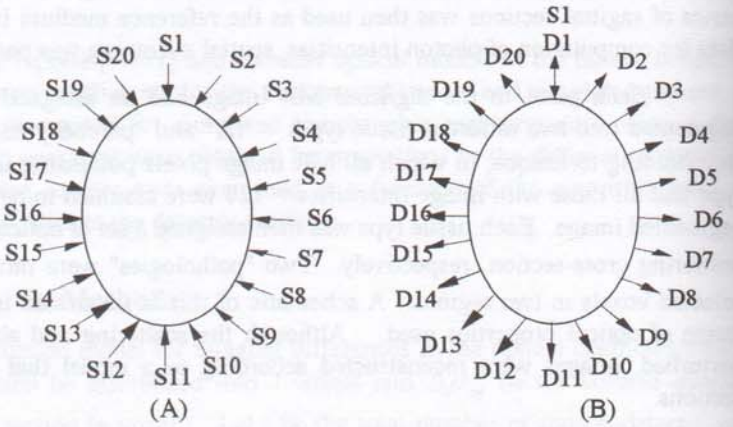

Figure 4. Illustration of source and detector locations for studies. (A) twenty source locations; (B) twenty detector locations for source S1.

where:

$$\Phi(\mathbf{r},t) = \int_{4\pi} \phi(\mathbf{r},\Omega,t)\,d\Omega,$$

$$S(\mathbf{r},t) = \int_{4\pi} s(\mathbf{r},\Omega,t)\,d\Omega,$$

$$D(\mathbf{r}) = \frac{1}{3(\mu_a(\mathbf{r}) + \mu_s'(\mathbf{r}))} = \frac{1}{3(\mu_a(\mathbf{r}) + \mu_s(\mathbf{r})(1-g))},$$

$$g = \frac{\int_{4\pi} \mu_s(\mathbf{r},\Omega'\cdot\Omega)\Omega'\cdot\Omega\,d\Omega}{\int_{4\pi} \mu_s(\mathbf{r},\Omega'\cdot\Omega)\,d\Omega} = \frac{\int_0^{\pi} \mu_s(\mathbf{r},\cos\theta)\cos\theta\sin\theta\,d\theta}{\int_0^{\pi} \mu_s(\mathbf{r},\cos\theta)\sin\theta\,d\theta},$$

and g is the average value of the cosine of the scattering angle. The grid size chosen for a particular computation varied with the type of optical parameters chosen. In general, an effort was made to choose grid sizes smaller than the largest value for μ_s^{-1}. In some cases, due to computational limitations, this was not practical and larger grid sizes were adopted. We are aware that this may lead to some errors in the accuracy of the computed results, but for the purposes of these computations, such errors should not affect the validity of the reconstruction results. Because different grid sizes were used in the direct problem, the corresponding volume of the breast considered also varied. In effect, we have evaluated a series of breasts that have identical anatomy but are scaled to different sizes. Table 2 shows the specific parameters used to compute solutions to the forward problem for each of the breast types examined. For purposes of comparison, results obtained from direct problems having dimension of 98x70x48 were subsequently spatially averaged to a grid size of

Table 1: List of optical coefficients assigned to segmented MR images.

Type	Fat		Parenchyma		Tumor	
	μ_a mm^{-1}	μ_s mm^{-1}	μ_a mm^{-1}	μ_s mm^{-1}	μ_a mm^{-1}	μ_s mm^{-1}
I	0.003	0.20	0.01	0.30	0.05	0.50
II	0.006	0.40	0.02	0.60	0.10	1.00
III	0.012	0.40	0.04	0.60	0.10	1.00
IV	0.012	0.40	0.04	0.60	0.01	0.10
V	0.01	1.00	0.03	0.50	0.50	3.00
VI	0.01	2.00	0.03	1.00	0.50	6.00
VII	0.01	4.00	0.03	2.00	0.50	12.00

Table 2: Parameters used for solution of direct problem

Type	Problem Size	Voxel Length (mm)	Δt (sec)	Breast Volume (cm^3)	Tumor Volume (cm^3)
I	$98\times70\times48$	1.75	7×10^{-13}	~1590	1.16
II	$98\times70\times48$	0.9	7×10^{-13}	~215	0.16
III	$98\times70\times48$	0.9	7×10^{-13}	~215	0.16
IV	$98\times70\times48$	1.75	4×10^{-13}	~1590	1.16
V	$49\times35\times24$	2.7	4×10^{-12}	~730	0.53
VI	$49\times35\times24$	2.7	1.5×10^{-11}	~730	0.53
VII	$98\times70\times48$	1.35	6×10^{-12}	~730	0.53

49x35x24 before attempting image recovery. The tumor size for the direct problem was also scaled such that for the large size array it measured 6x6x6 and 3x3x3 for the small size array.

A schematic of the tomographic measurement scheme used for data collection is shown in Figure 4. Twenty sources were placed at the boundary of the breast and twenty detector readings were obtained for each source, for all reference and pathology–containing media. The position of the sources and detector were confined to a plane located half-way between the chest wall and nipple, parallel to the chest wall and bisected the tumors. The normalized photon intensity in each voxel was also recorded for the reference medium in each set for weight matrix calculations.

Image Reconstruction

Three iterative algorithms – (1) projection onto convex sets (POCS) [12], (2) conjugate gradient descent (CGD) [13], and (3) simultaneous algebraic reconstruction algorithm (SART) [14], all based on the perturbation model, were used for image reconstruction. POCS is a sequential projection method which reaches the intersection point of L constraint sets by projecting the current estimate of the solution onto each set C_l (a set which satisfies the l^{th} constraint), l = 1,2, ... ,L, sequentially and iteratively. Letting $\underline{\Delta \mathbf{x}^n}$ represent the estimate at the n^{th} iteration, each step in POCS can be represented by:

$$\Delta \mathbf{x}^{n+1} = P_L \circ P_{L-1} \circ \ldots \circ P_1 \Delta \mathbf{x}^n. \tag{3}$$

Here, P_l represents the projection operator onto C_l, such that $\underline{P_l \Delta \mathbf{x}^n}$ is the element in C_l that is closest to $\underline{\Delta \mathbf{x}^n}$. Youla [15] has proved that, as long as the intersection of the constraint sets is not empty, iterative projections onto these sets will converge to their intersection. The CGD update is computed according to the conjugate gradient direction $\mathbf{d}^n$:

$$\mathbf{d}^n = -\mathbf{g}^n + \beta^n \mathbf{d}^n, \quad \text{where} \quad \beta_n = \frac{\left\|\mathbf{g}^n\right\|^2}{\left\|\mathbf{g}^{n-1}\right\|^2}, \quad \mathbf{g}^n = \frac{\partial E}{\partial \Delta \mathbf{x}} = \mathbf{W}^T \cdot (\Delta \mathbf{I}^n - \Delta \mathbf{I}),$$

$$\Delta \mathbf{I}^n = \mathbf{W} \cdot \Delta \mathbf{x}^n, \quad \Delta \mathbf{x}^{n+1} = \Delta \mathbf{x}^n - \alpha^n \mathbf{d}^n, \quad \alpha^n = \frac{{\mathbf{g}^n}^T \cdot \mathbf{d}^n}{\left\|\mathbf{W} \cdot \mathbf{d}^n\right\|^2}. \tag{4}$$

where $\mathbf{g}^n$ is the gradient vector, and α is called the step-size, which must be chosen appropriately to guarantee convergence. Theoretically, this algorithm should converge after a number of iterations less than or equal to the number of unknowns. The SART algorithm updates the reconstruction as follows:

$$\Delta x_j^{n+1} = \Delta x_j^n + \frac{\dfrac{\Delta I_i - \sum_j w_{ij} \cdot \Delta x_j^n}{\sum_j w_{ij}}}{\sum_i w_{ij}} \tag{5}$$

where i is the source–detector pair index, j the voxel index, and n the iteration number. We chose the SART algorithm because of its tendency to enhance image features in regions where all the w_{ij} are small.

2–D reconstructions (forcing the image to be symmetric in the direction perpendicular to the plane defined by the sources and detectors) were performed. Two range constraints were applied: positive range constraint on reconstruction results and positive range constraint on detector readings. Range constraints on detector readings were imposed prior to reconstruction, with all the negative readings set to zero: $\Delta\phi_i = 0$ if $\Delta\phi_i < 0$. Where indicated, additive white Gaussian noise was added to the computed $\Delta\phi_i$ values. The range constraints on reconstruction results were imposed after each iteration: $\Delta\mu_{aj}^n = 0$ if $\Delta\mu_{aj}^n < 0$.

3. Results

Figure 5 shows a plot of the logarithm of computed photon intensities in several sagittal views for a source directed normal to the tissue in the region of the nipple (left side). The particular case is based on Type V background conditions. Figures 5a shows the result for the reference medium without added tumors, and 5b for when two tumors are added. The two darken structures in slice y17 indicate the position of the added tumors. The jagged edge on the left side of the figures illustrates the detected edge of the tissue for the particular thresholding values chosen and does not represent any error in solution of the forward problem.

Figure 5

(A) Reference Medium

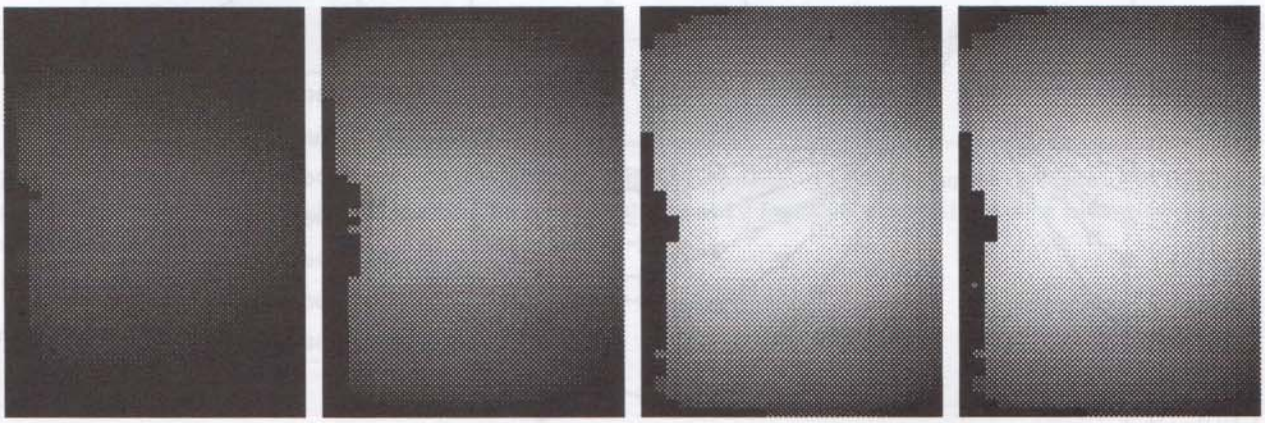

y10 y15 y17 y20

(B) Medium Containing Two Pathologies

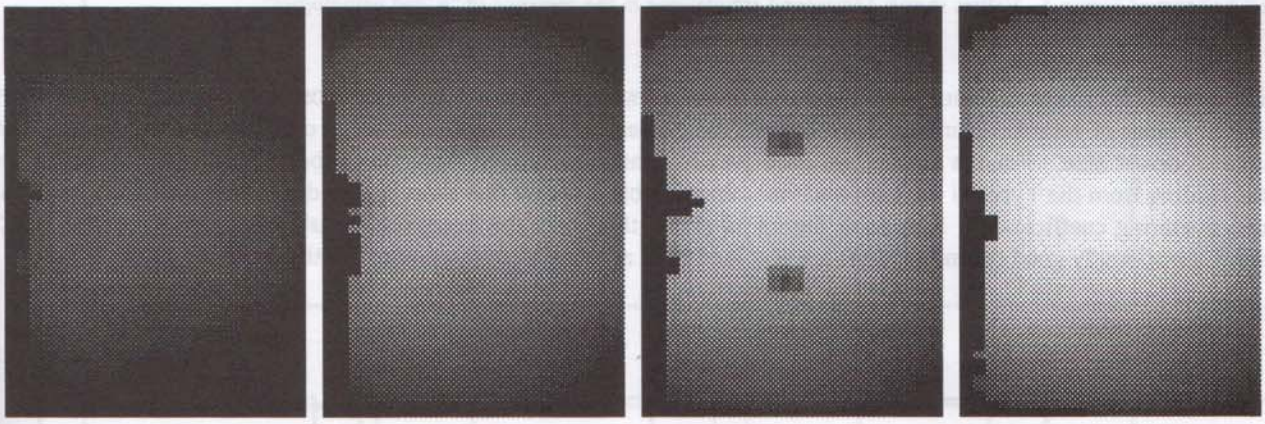

y10 y15 y17 y20

Figure 5. Slices displayed were selected from a set of 35 derived from solution of the forward problem. Note the presence of the added "tumors" in slice y17.

Data shown in Figure 6 are the computed detector responses for each of the background conditions tested for a source located at position 6. Inspection reveals that, as expected, a large range of intensity values are obtained with the detector located opposite the source having usually the lowest values. Comparison of these values to allowable source intensities indicates that only Type VII medium yields values that are are sufficiently low to be effectively unmeasureable. Background medium Types V and VI are within the range reported for breast tissue [17] and the others represent values that likely underestimate the transport scattering lengths.

Figure 7 shows the results of 2-D reconstructions using the CGD algorithm for each of the different test media after 1000 iterations. In all cases both tumors are well resolved and their spatial location is correctly identified. Figure 8 shows the quality of the reconstruction for Types V-VII media as a function of iteration number. Acceptable results are

seen after only 10 iterations which corresponds to approximately 2 minutes of CPU time using a 486 PC. A comparison of image quality achieved using the different algorithms as a function of iteration number for the Type VI medium is shown in Figure 9. It is evident that there are considerable differences in image quality with POCS < CGD ≈ SART. Results shown in Figures10 and 11 examine the effect that systematic errors in the weight function have on image quality as a function of algorithm used. We consider this as it is appreciated that, in practice, knowledge of the correct weight

Figure 6

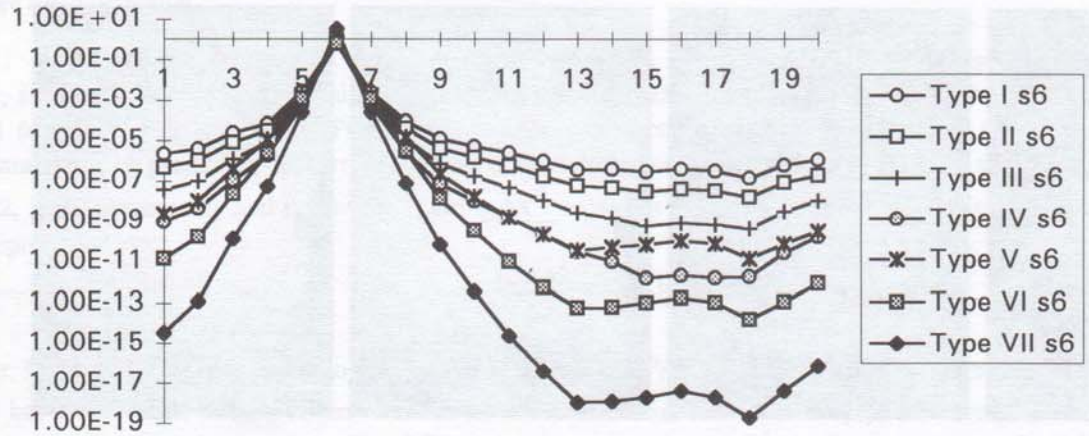

Figure 6. Computed surface intensity values for the different assigned values of optical coefficients listed in Table 1 for source position 6 shown in Figure 4. Values shown correspond simulations in the presence of "added pathologies".

function is itself an unknown. Thus, it is likely that only an approximation can be made. For these computations we have modeled two types of systematic errors; inaccuracy in assignment of background scattering coefficients and inaccuracy in estimates of breast size. For the former we used weight functions derived from the Type V medium to evaluate the detector reading from the Type VI medium and vice versa. Table 1 shows that these media differ only in the values of the assigned scattering coefficients. Results in Figure 10 show that, with the exception of data computed using the POCS algorithm, surprisingly good reconstructions are obtained even after only 10 iterations. For the latter we conducted a

Figure 7.

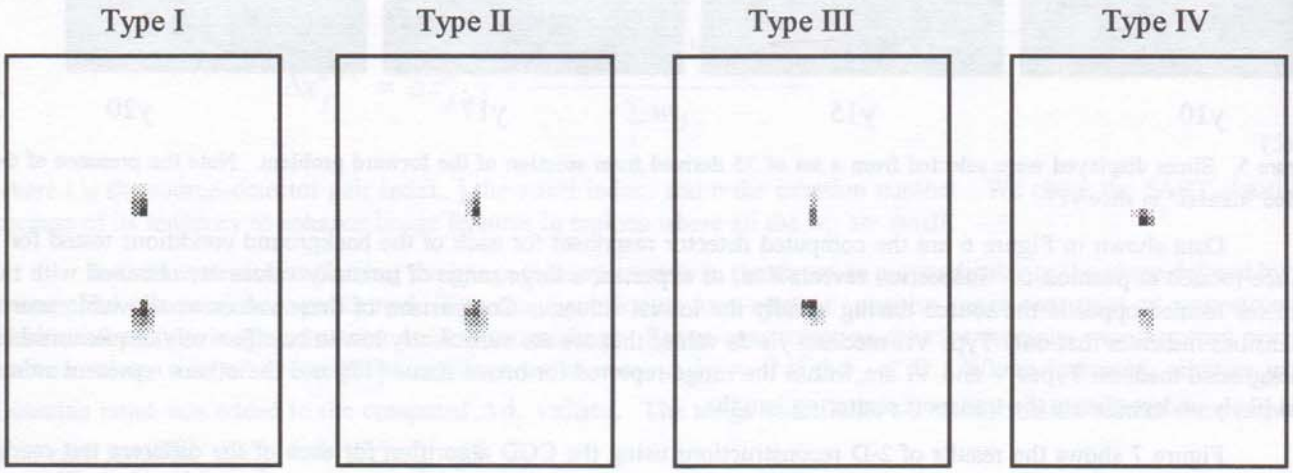

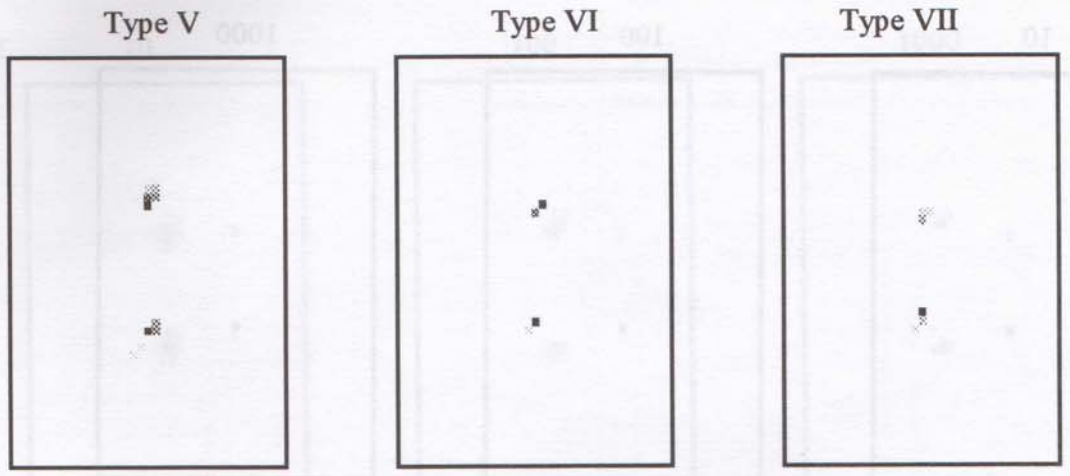

Figure 7. Reconstructed images of MR-segmented data sets with added tumors. Results shown were obtained after 1000 iterations using the CGD algorithm in the absence of added noise. See Tables 1 and 2 for listing of optical and other parameters for solution of the forward problem.

Figure 8.

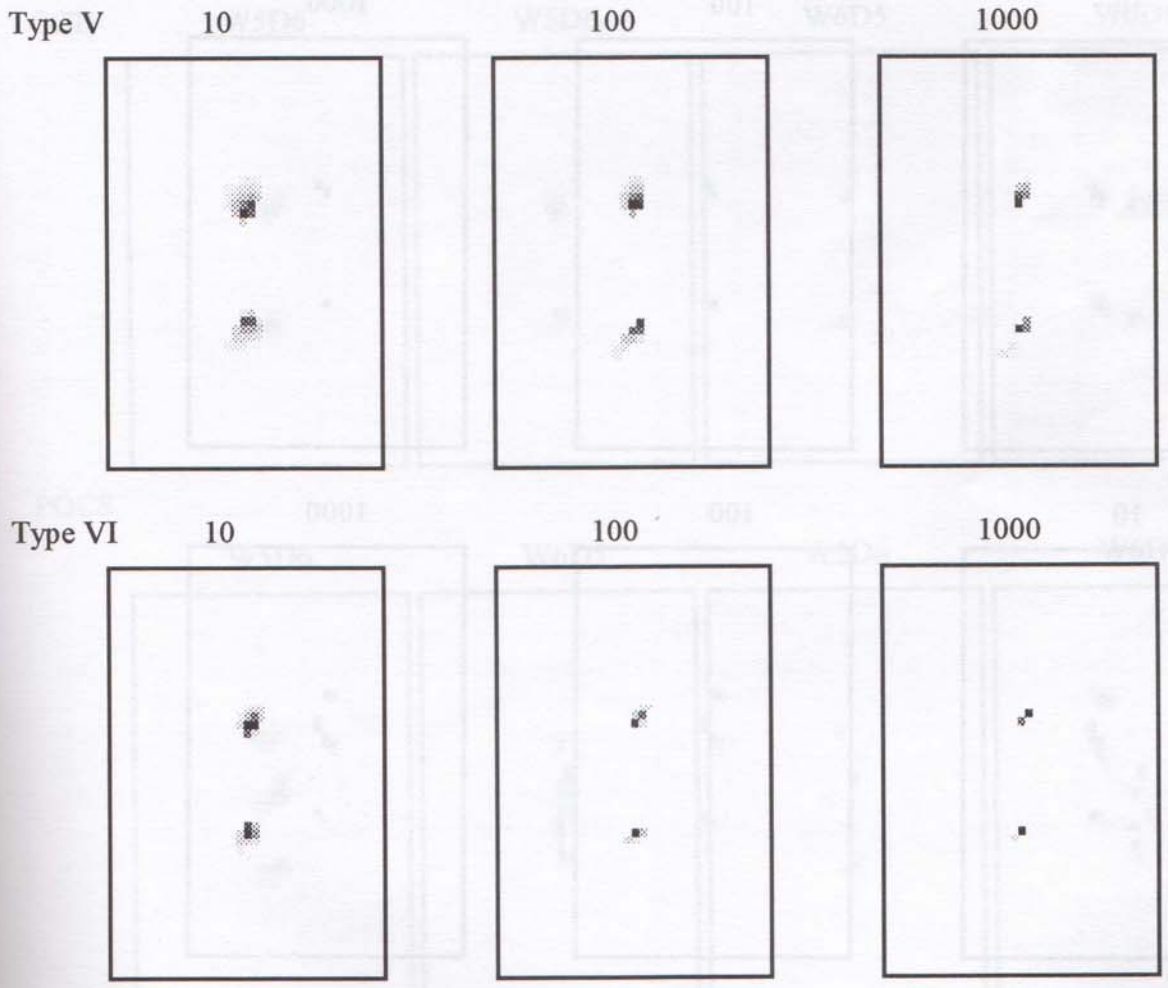

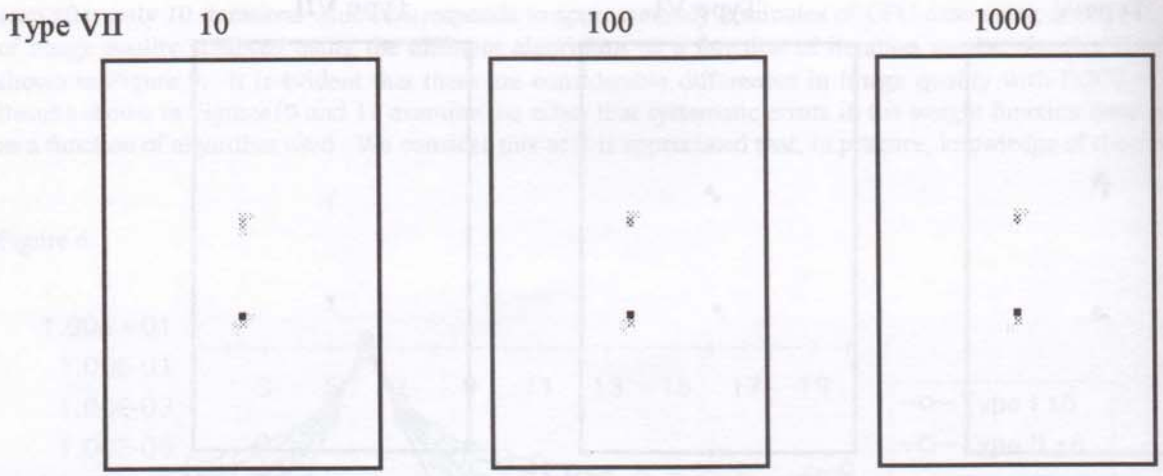

Figure 8. Reconstructed images obtained for Types V-VII media in the absence of added noise after the indicated number of iterations using the CGD algorithm.

Figure 9

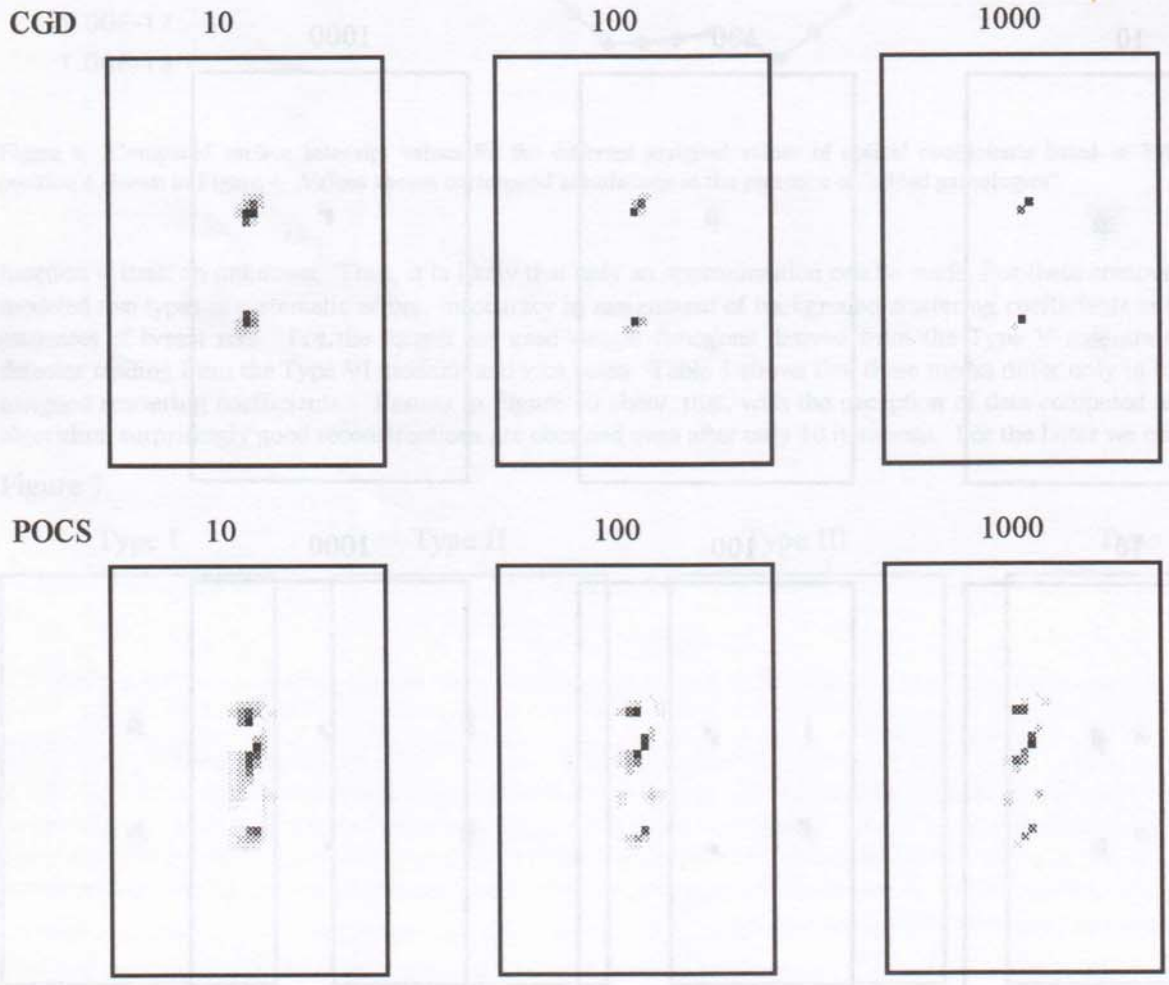

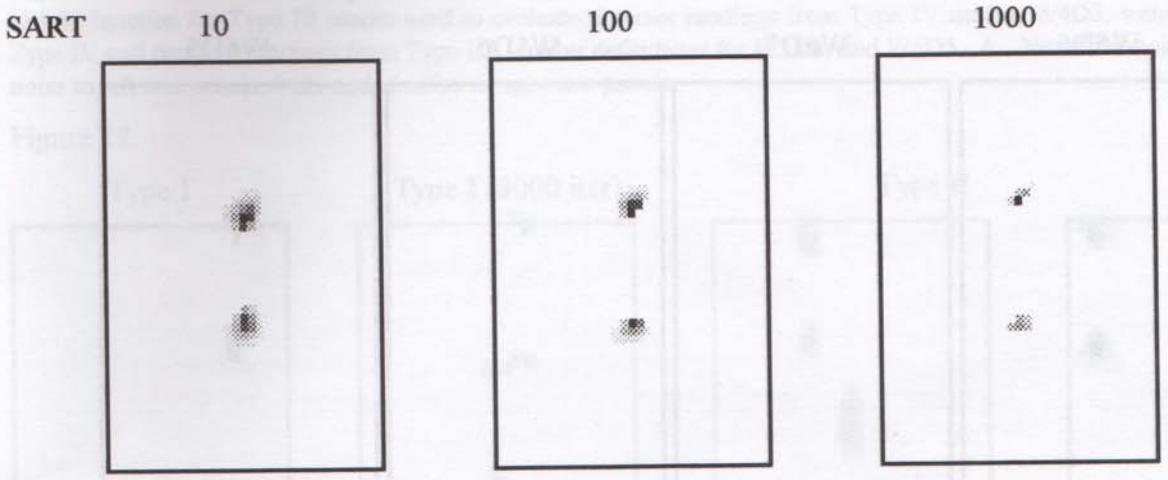

Figure 9 Reconstructed images obtained of Type VI media using the CGD, POCS and SART algorithms in the absence of added noise after the indicated number of iterations.

Figure 10.

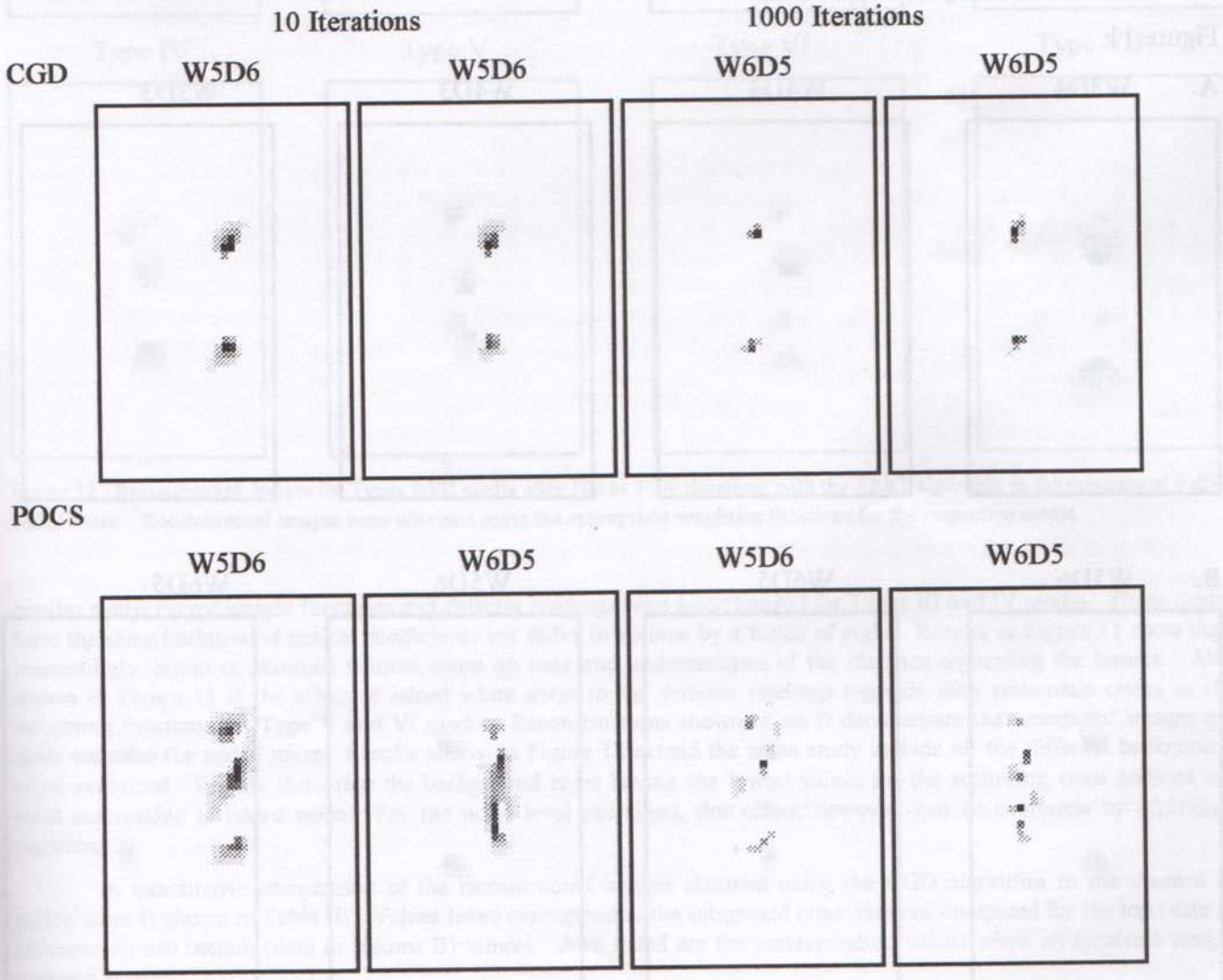

SART

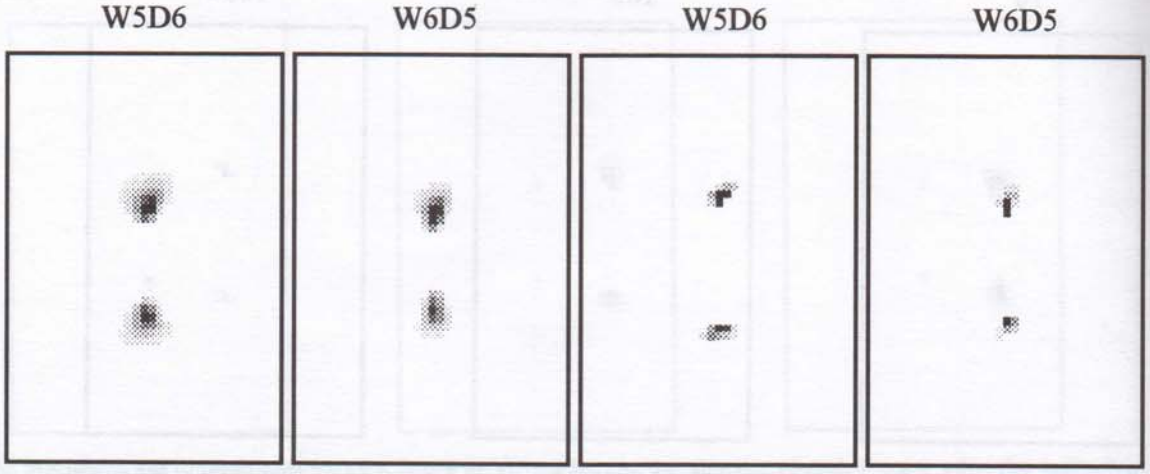

Figure 10. Effect of systematic error in weighting functions. Reconstructed images obtained are for Types V and VI media calculated using the CGD, POCS and SART algorithms in the absence of added noise after 10 and 1000 iterations. Abbreviations used: W5D6, weight function computed for Type V media used to evaluate detector readings from Type VI media.; W6D5, weight function for Type VI media and detector readings from Type V media.

Figure 11.

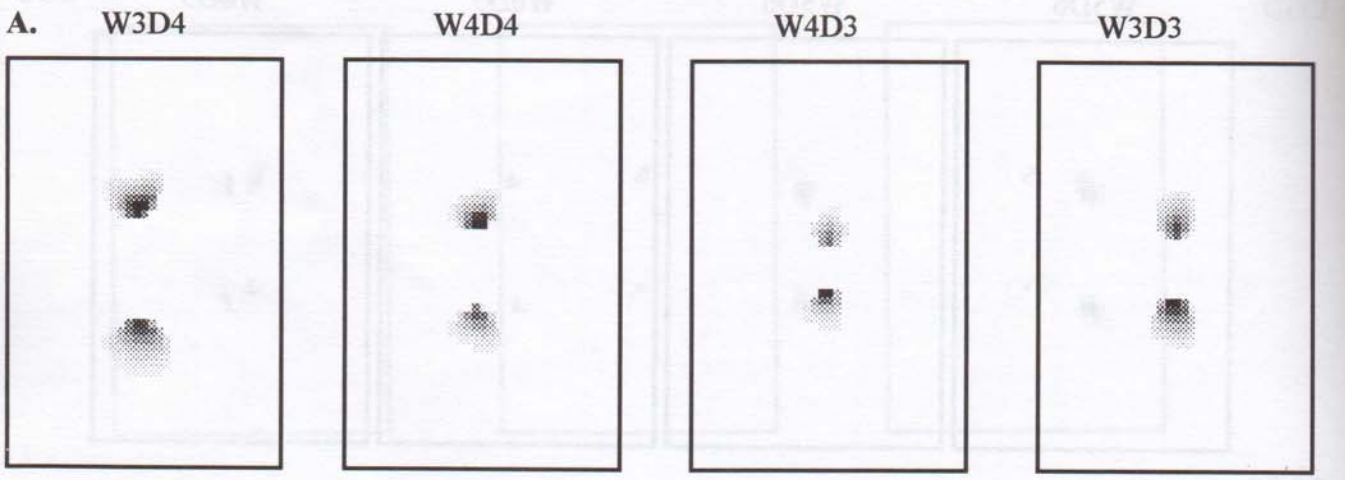

Figure 11. Reconstructed images obtained using the SART algorithm after 100 iterations. Abbreviations used: W3D4, weight function for Type III media used to evaluate detector readings from Type IV media; W4D3, weight functions for Type IV and detector readings from Type III; similar definitions for W5D6, and W6D5. **A.** No added noise; **B.** No added noise to left two panels, 0 dB added noise to right two panels.

Figure 12.

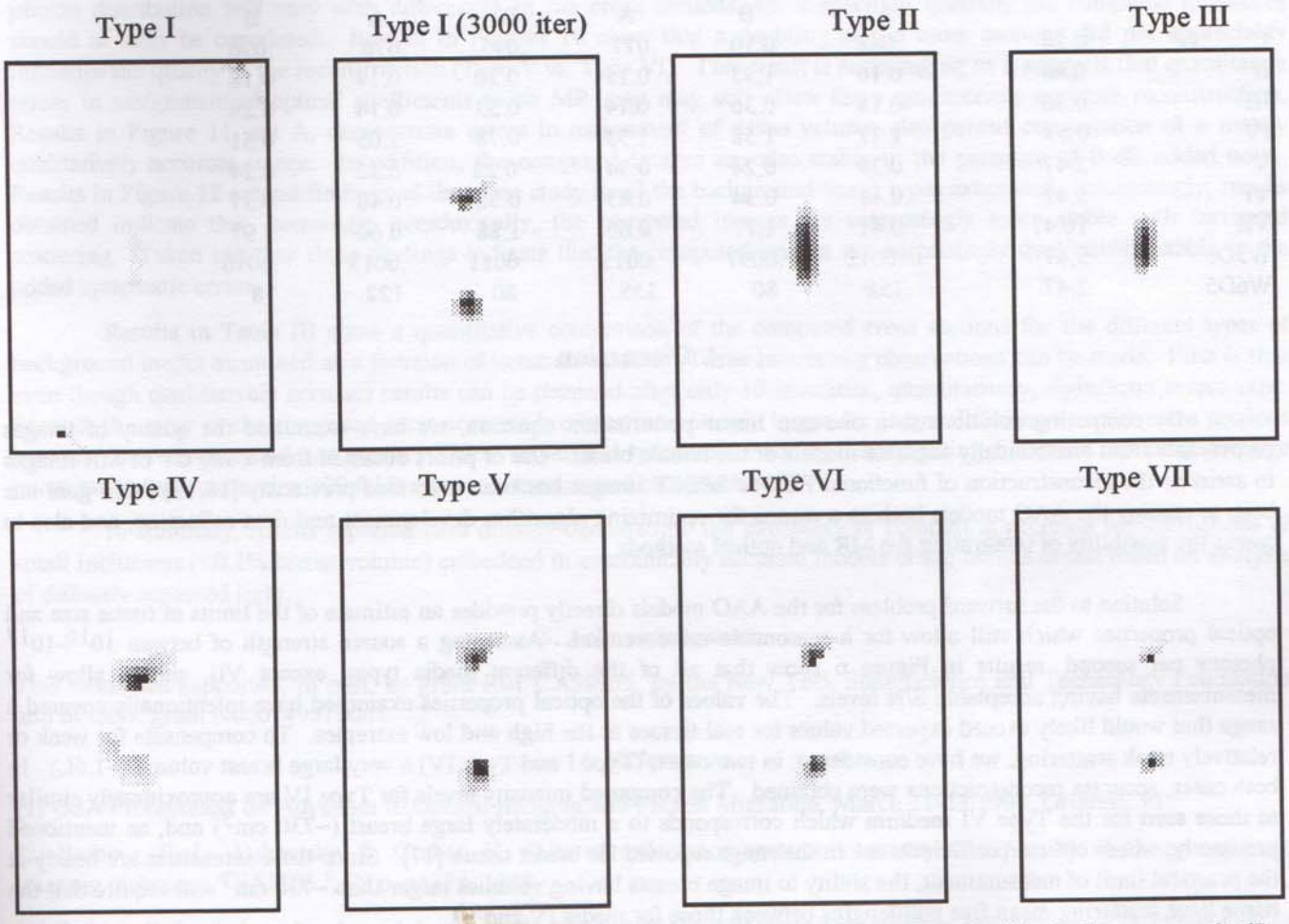

Figure 12. Reconstructed images for Types I-VII media after 100 or 3000 iterations with the SART algorithm in the presence of 0 dB added noise. Reconstructed images were obtained using the appropriate weighting functions for the respective media.

similar study, except weight functions and detector readings were interchanged for Types III and IV media. These media have the same background optical coefficients but differ in volume by a factor of eight. Results in Figure 11 show that, interestingly, errors in assumed volume cause an over and underestimate of the distance separating the tumors. Also shown in Figure 11 is the effect of added white noise to the detector readings together with systematic errors in the weighting functions for Type V and VI media. Reconstructions shown in set B demonstrate that computed images are quite stable to the added noise. Results shown in Figure 12 extend the noise study include all the different background types examined. Results show that the background types having the lowest values for the scattering cross sections are most susceptable to added noise. For the noise level examined, this effect, however, can be overcome by additional iterations.

A quantitative comparison of the reconstructed images obtained using the CGD algorithm in the absence of added noise is shown in Table III. Values listed correspond to the integrated cross sections computed for the top (data in columns A) and bottom (data in colums B) tumors. Also listed are the corresponding values when an incorrect weight function is used.

Table III

Quantitative Comparison of Reconstruction Results
(CGD, No Noise)

Type	$\Delta\Sigma$ Actual (mm^{-1})	$\Delta\Sigma$ Computed (mm^{-1}) (No. of Iterations)					
		10		100		1000	
		A	B	A	B	A	B
I	0.24	.088	0.10	.077	.095	.076	.096
II	0.48	0.16	1.93	0.15	0.20	0.14	0.18
III	0.46	0.18	0.36	0.14	0.33	0.14	0.28
IV	-0.53	1.17	1.58	1.33	0.78	1.05	0.51
V	2.47	0.39	0.24	0.34	0.22	0.32	0.24
VI	5.47	0.48	0.34	0.43	0.32	0.48	0.37
VII	10.47	0.41	1.77	0.60	1.88	0.60	1.97
W5D6	5.47	.0012	.0097	.0013	.0011	.0013	.0010
W6D5	2.47	158	80	155	80	122	78

4. Discussion

By computing solutions to a one-step linear perturbation equation, we have examined the quality of images recoverable from anatomically accurate models of the female breast. Use of priors obtained from x-ray CT of MR images to assist in the reconstruction of functional PET or SPECT images has been described previously [18,19]. Our goal has been to employ the AAO models both as a means for optimizing algorithm development and data collection, and also to assess the feasibility of integrating the MR and optical methods.

Solution to the forward problem for the AAO models directly provides an estimate of the limits of tissue size and optical properties which still allow for a reasonable measurement. Assuming a source strength of betwen 10^{16}-10^{17} photons per second, results in Figure 6 show that all of the different media types, except VII, should allow for measurements having acceptable S/N levels. The values of the optical properties examined have intentionally covered a range that would likely exceed expected values for real tissues at the high and low extremes. To compensate for weak or relatively weak scattering, we have considered, in two cases, (Type I and Type IV) a very large breast volume (~1.6L). In both cases, accurate reconstructions were obtained. The computed intensity levels for Type IV are approximately similar to those seen for the Type VI medium which corresponds to a moderately large breast (~730 cm^3) and, as mentioned previously, whose optical coefficients are in the range reported for breast tissue [17]. Since these intensities are nearly at the practical limit of measurement, the ability to image breasts having volumes larger than ~730 cm^3 will require that the tissue have scattering mean free pathlengths between those for media IV and VI.

In all cases but medium IV, the values of the optical cross-sections for the "added tumors" exceeded those of the background medium. For media types I-III, the relative difference was less for scattering than absorption. The cross sections for medium Type II are double those of medium I. For medium Type III, the values of the absorption cross section for the background tissues are doubled compared to medium Type II. Media Types V-VII have much larger values for the scattering cross sections of which the latter two have been doubled and doubled again, respectively, compared to medium Type V. In all these cases, for which breast size, absolute value of the optical cross sections and their contrast between the added tumors and background tissues were varied, we observed that good quality reconstructions were obtained, particularly for the CGD and SART algorithms.

Reconstruction results for the Type IV medium are particularly interesting. A perturbation having smaller values in the optical coefficients compared to the reference medium will cause some of the ΔI values to have a negative values. As indicated in Methods, we employ positivity constraints on both the detector readings and reconstruction results. Then, how is it that a seemingly accurate qualitative map of the difference in cross sections can be obtained? The answer lies in the observation that a difference in the scattering cross section will cause a redistribution of photon intensities, such that some detectors see more photons and others less. It would appear that sufficient spatial information exists in the more limited positive ΔI values to permit an accurate reconstruction. In addition, because we have made no explicit attempt to

separately compute images for differences in absorption and scattering, we interpret the computed maps as being proportional to the difference in the absolute value of the total cross section.

There are several sources of errors that can influence the reconstruction results. Here we have examined the effect of systematic errors in the weight functions and added white noise. For the former we have used weight functions computed from one medium to evaluate detector readings obtained from another. The rationale for this is that whereas photon distribution will vary with differences in the cross sections, for a specified anatomy the computed intensities should at least be correlated. Results in Figures 10 show that a doubling of the cross sections did not appreciably influence the quality of the reconstruction (Type V vs. Type VI). This result is encouraging as it suggests that quantitative errors in assignment of optical coefficients to an MR map may still allow for a qualitatively accurate reconstruction. Results in Figure 11, set A, demonstrate errors in assignment of tissue volume also permit computation of a mostly qualitatively accurate image. In addition, the computed images are also stable in the presence of 0 dB added noise. Results in Figure 12 extend findings of the noise study to all the background tissue types examined. Interestingly, results obtained indicate that, seemingly paradoxically, the computed images are increasingly more stable with increased scattering. Taken together these findings indicate that the computed images are surprisingly qualitatively stable to the added systematic errors.

Results in Table III show a quantitative comparison of the computed cross sections for the different types of background media examined as a function of iteration number. Three interesting observations can be made. First is that even though qualitatively accurate results can be obtained after only 10 iterations, quantitatively, siginficant errors exist. Second, the error in the computed cross sections becomes increasingly larger for larger differences in the cross sections between the reference and test media. Third, a two fold systematic error in the weighting functions can produce large quantitative (approximatley 300 fold) error in the estimated cross sections.

In summary, results reported here directly demonstrate the capability of computing accurate reconstructions of small inclusions (<0.1% breast volume) embedded in anatomically accurate models of the female breast based on analysis of diffusely scattered light.

5. Acknowledgments

This work was supported, in part, by grant R01 CA59955, by the New York State Science and Technology Foundation and by ONR grant N000149510063.

6. References

[1] OSA Proceedings on Advances in Optical Imaging and Photon Migration, March 21-23 1994, Orlando, Fl.

[2] Barbour, R. L., Lubowsky, J., Graber, H., "Use of reflectance spectrophotometry as a possible 3–D spectroscopic imaging technique," FASEB J., 2, p. a1772, 1988.

[3] Barbour R. L., Lubowsky, J., and Aronson, R., *Method of imaging a random medium*, US. Patent no. 5,137,355 (filed June 8, 1988; issued August 11, 1992).

[4] Singer, J. R., Grünbaum, F. A., Kohn, P., Zubelli, J. P., "Image reconstruction of the interior of bodies that diffuse radiation," Science, 248, pp. 990–993, 1990.

[5] Arridge, S. R., van der Zee, P., Cope, M. and Delpy, D. T., "Reconstruction methods for infra–red absorption imaging." SPIE 1431, pp. 204–215, 1991.

[6] Barbour, R. L., Graber, H. L., Wang, Y., Chang, J., Aronson, R., "A perturbation approach for optical diffusion tomography using continuous wave and time resolved data," in *Medical Optical Tomography: Functional Imaging and Monitoring*, SPIE Inst. IS11, pp. 87–120, 1993.

[7] Arridge, S. R., "The forward and inverse problems in time resolved infra–red imaging," in *Medical Optical Tomography: Functional Imaging and Monitoring*, SPIE Inst. IS11, pp. 35–64, 1993.

[8] J. G. Webster, ed., *Electrical impedance Tomography*, Adam Hilger, Bristol, 1990.

[9] J. G. Berryman, "Stable iterative reconstruction algorithm for nonlinear traveltime tomography," *Inverse Problems*, vol. 6, pp. 21–42, 1990.

[10] Chang, J., Graber, H. L., Koo, P.C., Aronson, R., Barbour, S.S., and Barbour, R. L., (1994) "Progress toward optical mammography: Imaging in dense scattering media using time-independent sources". IEEE Medical Imaging Conference, Norfolk, VA, Nov 3-5, 1994, *in press*.

[11] R L. Barbour, J. Chang, H. L. Graber, P.C. Koo, R. Aronson and S. S. Barbour, "MR Assisted Optical Mammography", U. of Penn. Conference on Integration of Medical Optical Imaging and Spectroscopy (MOI/MOIS) and Magnetic Resonance Imaging (MRI), Philadelphia, PA, Dec., 1994.

[12] P.C. Koo, F. H. Schlereth, R. L. Barbour and H. L. Graber, "Efficient numerical method for quantifying photon distributions in the interior of thick scattering media", in OSA Proc. Advances in Optical Imaging and Photon Migration, vol. 21, pp 187-192, 1994.

[13] D. C., Youla and H. Webb, "Image restoration by the method of convex projections onto convex sets– Part I", IEEE Trans. Med. Imaging, vol. MI–1, pp. 81–94, 1982.

[14] P. E. Gill, W. Murray, and M. H. Wright, Practical Optimization. New York: Academic Press, 1981.

[15] A. H. Anderson, A. C. Kak, "Simultaneous algebraic reconstruction technique (SART): A superior implementation of the ART algorithm", Ultrasonic Imag., 6, pp. 81–94, 1984.

[16] D. C. Youla, "Mathematical Theory of Image Reconstruction", *Image Recovery: Theory and Application*, Henry Stark, ed., New York, Academic Press, 1987.

[17] Cheong, W. F., Prahl, S. A., and Welch, A. J. "A review of the optical properties of biological tissues," *IEEE J. Quantum Elec.* 26, 2166–2185, 1990.

[18] G. Gindy, M. Lee, A. Rangarajan, and I. G. Zubal, "Bayesian reconstruction of functional images using anatomical information as priors," IEEE Trans. Med. Imag., vol. 12, pp. 670-680, 1993.

[19] R. Leahy, and X. Yan, "Incorporation of anatomical MR data for improved functional imaging with PET", Information Processing in Medical Imaging. New York, NY: Springer-Verlag, 1991, pp. 105-120.